Supplementary information for "Quantum speed limit for complex dynamics"

Mao Zhang, Huai-Ming Yu, and Jing Liu*
National Precise Gravity Measurement Facility, MOE Key Laboratory of Fundamental Physical Quantities Measurement, School of Physics, Huazhong University of Science and Technology, Wuhan 430074, China

This is the supplementary information for the paper "Quantum speed limit for complex dynamics", which includes the thorough derivations and calculations of the results in the main text.

I. THE OQSL FOR TIME-DEPENDENT HAMILTONIAN WITH TIME-INDEPENDENT EIGENSTATES

A. Proof of Theorem 1

Consider the time-dependent Hamiltonian of the form

$$H(t)=\sum_i E_i(t)\left|E_i\right\rangle\left\langle E_i\right|, \tag{1}$$

where the energies are assumed to be ordered ascendingly, i.e., $E_0(t)\leq E_1(t)\leq\cdots\leq E_{N-1}(t)$ (not all the equalities are saturated simultaneously) and $|E_i\rangle$ is independent of the time for any subscript i. With this Hamiltonian, the OQSL τ satisfies

$$\int_0^\tau E_{N-1}(t)-E_0(t)\mathrm{d}t=\Theta, \tag{2}$$

where $E_{N-1}(t)$ and $E_0(t)$ are the highest and lowest energies of the Hamiltonian at time t. The proof is as follows.

In the Bloch representation, any N-dimensional density matrix ρ can be expressed by

$$\rho=\frac{1}{N}\left(\mathbb{1}+\sqrt{\frac{N(N-1)}{2}}\vec{r}\cdot\vec{\lambda}\right), \tag{3}$$

where $\vec{\lambda}$ is the vector of SU(N) generators, $\vec{r}$ is the Bloch vector satisfying $|\vec{r}|\leq 1$ and $\mathbb{1}$ is the identity matrix. In the case of unitary dynamics, any SU(N) generator satisfies $U(t)\lambda_i U^\dagger(t)=\sum_j C_{ij}(t)\lambda_j$ with $U(t)$ a unitary operator, then the dynamics of $\vec{r}$ can be written as $\vec{r}(t)=C^{\mathrm{T}}(t)\vec{r}$. Utilizing the relation $\mathrm{Tr}(\lambda_i\lambda_j)=2\delta_{ij}$ with δ_{ij} the Kronecker delta function, $C_{ij}(t)$ can be further solved as $C_{ij}(t)=\mathrm{Tr}(U(t)\lambda_i U^\dagger(t)\lambda_j)/2$.

With the Hamiltonian (1), the unitary operator can be expressed by

$$\begin{aligned}U(t)&=e^{-i\sum_m\int_0^t E_m(t_1)\mathrm{d}t_1\left|E_m\right\rangle\left\langle E_m\right|}\\&=\sum_m e^{-i\int_0^t E_m(t_1)\mathrm{d}t_1}\left|E_m\right\rangle\left\langle E_m\right|,\end{aligned} \tag{4}$$

which indicates

$$C_{ij}(t)=\frac{1}{2}\sum_{mn}e^{i\int_0^t E_m(t_1)-E_n(t_1)\mathrm{d}t_1}[\lambda_i]^*_{mn}[\lambda_j]_{mn} \tag{5}$$

with $[\lambda_j]_{mn}$ the mnth entry of λ_j. In the energy basis $\{|E_0\rangle,|E_1\rangle,\ldots,|E_{N-1}\rangle\}$, $C(t)$ has the same structure with the time-dependent Hamiltonian [1], i.e.,

$$C(t)=\bigoplus_{n=1}^{N-1}V(n,t), \tag{6}$$

where $V(n,t)=\left[\bigoplus_{i=0}^{n-1}M(\Delta_{ni})\right]\bigoplus 1$ with

$$M(x)=\begin{pmatrix}\cos x & -\sin x\\ \sin x & \cos x\end{pmatrix} \tag{7}$$

and $\Delta_{ni}=\int_0^t E_n(t_1)-E_i(t_1)\mathrm{d}t_1$. Then the angle between the initial and evolved Bloch vectors is

$$\cos\theta=\frac{\vec{r}(t)\cdot\vec{r}}{|\vec{r}|^2}=\frac{\vec{r}^{\mathrm{T}}C(t)\vec{r}}{|\vec{r}|^2}. \tag{8}$$

Utilizing Eq. (6), it can be further calculated as

$$\cos\theta=1-\frac{1}{|\vec{r}|^2}\sum_{n=1}^{N-1}\sum_{i=0}^{n-1}[1-\cos(\Delta_{ni})](r^2_{n^2+2i-1}+r^2_{n^2+2i})$$

with r_i the ith element of $\vec{r}$. Hence, the set $\mathcal{S}$ can be directly expressed by

$$\begin{aligned}\mathcal{S}=\Big\{\vec{r}\,\Big|\,1-\cos\Theta=\frac{1}{|\vec{r}|^2}\sum_{n=1}^{N-1}\sum_{i=0}^{n-1}[1-\cos(\Delta_{ni})]\\ \times\left(r^2_{n^2+2i-1}+r^2_{n^2+2i}\right),\exists t\Big\}.\end{aligned} \tag{9}$$

To further obtain the OQSL, the two-step proof strategy used in Appendix B in Ref. [1] needs to be applied. Define

$$f(t):=\frac{1}{|\vec{r}|^2}\sum_{n=1}^{N-1}\sum_{i=0}^{n-1}[1-\cos(\Delta_{ni})](r^2_{n^2+2i-1}+r^2_{n^2+2i}).$$

Substituting the equation

$$\int_0^\tau E_{N-1}(t)-E_0(t)\mathrm{d}t=\Theta \tag{10}$$

into the expression of $f(t)$, it can be seen that

$$\left.\frac{\partial f(t)}{\partial t}\right|_{t=\tau}\geq 0, \tag{11}$$

which indicates τ is in the first monotonic increasing regime of $f(t)$. In the meantime, it can also be found

that $f(\tau) \leq 1-\cos\Theta$. If the solution of $f(t) = 1-\cos\Theta$ is not in the first increasing regime of $f(t)$, then t is obviously larger than τ; if this solution is in the first increasing regime, then due to $f(\tau) \leq 1-\cos\Theta = f(t)$ one can also see that $t \geq \tau$. Hence, τ is a lower bound of the time to reach the target angle.

Now we discuss the optimal probe states to reach the OQSL. To let the equation $1-\cos\Theta = f(\tau)$ holds, the term $r^2_{n^2+2i-1} + r^2_{n^2+2i}$ for the subscripts n, i satisfying $\Delta_{ni} \neq \int_0^\tau E_{N-1}(t) - E_0(t)\mathrm{d}t$ has to vanish. Further assume the degeneracy of the ground states and highest excited states are p and q, namely, $E_0(t) = E_1(t) = \cdots = E_{p-1}(t)$ and $E_{N-q}(t) = E_{N-q+1}(t) = \cdots = E_{N-1}(t)$, then it is easy to see that $r^2_{n^2+2i-1} + r^2_{n^2+2i}$ can only be nonzero when $n \in [N-q, N-1]$ and $i \in [0, p-1]$, which indicates that the optimal state is of the form

$$\sum_{i=0}^{N-1} \frac{1}{N} |E_i\rangle\langle E_i| + \sum_{\substack{k\in[0,p-1],\\ l\in[N-q,N-1]}} \xi_{kl} |E_k\rangle\langle E_l| + \xi^*_{kl} |E_l\rangle\langle E_k|, \tag{12}$$

where $\xi_{kl} = \sqrt{\frac{N-1}{2N}}(r_{l^2+2k-1} - i r_{l^2+2k})$. In the energy basis $\{|E_0\rangle, |E_1\rangle, \ldots, |E_{N-1}\rangle\}$, the state above can be written as

$$\frac{1}{N}\mathbb{1} + \begin{pmatrix} 0 & 0 & \xi \\ 0 & \cdots & 0 \\ \xi^\dagger & 0 & 0 \end{pmatrix}, \tag{13}$$

where $\mathbb{1}$ is a N-dimensional identity matrix, and ξ is a p by q matrix with klth entry ξ_{kl}. To make sure the density matrix is positive-semidefinite, according to the Schur complement theorem ξ needs to satisfy

$$\xi^\dagger \xi \leq \frac{1}{N^2}\mathbb{1}_q, \tag{14}$$

where $\mathbb{1}_q$ is a q-dimensional identity matrix. The theorem is then proved. ■

B. Example: two-level systems

Here we take a two-level system as a demonstration of Theorem 1. Consider the Hamiltonian

$$H(t) = f(t)\sigma_z, \tag{15}$$

where $f(t)$ is a function of time t, and σ_z is a Pauli Z matrix. In the Bloch representation, the evolved Bloch vector can be solved as

$$\begin{aligned} r_x(t) &= r_x \cos\left[2\int_0^t f(t_1)\mathrm{d}t_1\right] - r_y \sin\left[2\int_0^t f(t_1)\mathrm{d}t_1\right], \\ r_y(t) &= r_x \sin\left[2\int_0^t f(t_1)\mathrm{d}t_1\right] + r_y \cos\left[2\int_0^t f(t_1)\mathrm{d}t_1\right], \\ r_z(t) &= r_z, \end{aligned}$$

where $(r_x, r_y, r_z)^{\mathrm{T}} = \vec{r}$ is the Bloch vector of the initial state. Based on this dynamics, the angle between the initial and evolved states is

$$\cos\theta = \frac{\cos\left[2\int_0^t f(t_1)\mathrm{d}t_1\right](r_x^2 + r_y^2) + r_z^2}{|\vec{r}|^2}, \tag{16}$$

which indicates that the time to reach the target angle Θ satisfies the following equation

$$\sin^2\left[\int_0^t f(t_1)\mathrm{d}t_1\right] = \frac{|\vec{r}|^2}{|\vec{r}|^2 - r_z^2}\sin^2\left(\frac{\Theta}{2}\right). \tag{17}$$

Rewrite $\vec{r}$ into

$$\vec{r} = \eta(\sin\alpha\cos\varphi, \sin\alpha\sin\varphi, \cos\alpha)^{\mathrm{T}} \tag{18}$$

with $\eta \in [0,1]$, $\alpha \in [0,\pi]$ and $\varphi \in [0, 2\pi]$, and Eq. (17) reduces to

$$\sin^2\alpha = \frac{\sin^2\left(\frac{\Theta}{2}\right)}{\sin^2\left[\int_0^t f(t_1)\mathrm{d}t_1\right]}. \tag{19}$$

Now consider that $|\int_0^t f(t_1)\mathrm{d}t_1|$ is upper bounded by c_f, then in the case that $c_f < \Theta/2$, $\sin^2\left[\int_0^t f(t_1)\mathrm{d}t_1\right]$ is always less than $\sin^2(\Theta/2)$, which gives $\sin^2\alpha > 1$. This means no state can fulfill the target as $\sin^2\alpha$ is always equal or less than 1. In the case that $c_f \in [\Theta/2, \pi/2]$,

$$\sin^2\left[\int_0^t f(t_1)\mathrm{d}t_1\right] \leq \sin^2 c_f \leq 1. \tag{20}$$

Hence,

$$\sin^2\alpha \geq \frac{\sin^2\left(\frac{\Theta}{2}\right)}{\sin^2 c_f}, \tag{21}$$

indicating that the states that can fulfill the target satisfies $\alpha \in [\alpha_f, \pi - \alpha_f]$ with

$$\alpha_f = \arcsin\left(\frac{\sin\left(\frac{\Theta}{2}\right)}{\sin c_f}\right). \tag{22}$$

In the case that $c_f > \pi/2$, $\sin^2[\int_0^t f(t_1)\mathrm{d}t_1]$ can reach all the values between 0 and 1, and $\sin^2\alpha \geq \sin^2(\Theta/2)$, therefore, the states satisfies $\alpha \in [\Theta/2, \pi - \Theta/2]$. In a word, the set $\mathcal{S}$ can be expressed by

$$\mathcal{S} = \begin{cases} \emptyset, & c_f < \frac{\Theta}{2}, \\ \{\vec{r}\,|\,\alpha \in [\alpha_f, \pi-\alpha_f]\}, & c_f \in [\frac{\Theta}{2}, \frac{\pi}{2}], \\ \{\vec{r}\,|\,\alpha \in [\frac{\Theta}{2}, \pi - \frac{\Theta}{2}]\}, & c_f > \frac{\pi}{2}. \end{cases} \tag{23}$$

Here $\emptyset$ is the empty set, and in the second and third circumstances $\eta \in (0,1]$ and $\varphi \in [0, 2\pi]$.

With respect to the OQSL, due to the fact that the eigenvalues are always $f(t)$ and $-f(t)$, the maximum and

minimum ones are always $|f(t)|$ and $-|f(t)|$, respectively. Based on Theorem 1, the OQSL τ then satisfies

$$\int_0^\tau |f(t)|\mathrm{d}t = \frac{\Theta}{2}. \tag{24}$$

A physical example for the Hamiltonian (15) is the energy splitting coming from Zeeman effect, i.e.,

$$f(t) = -\frac{g\mu_\mathrm{B}}{2}B(t) \tag{25}$$

with g the Lande factor and μ_B the electron magnetic moment. $B(t)$ is the time-dependent magnetic field. For a periodic magnetic field $B(t) = B\cos(\omega t)$ with $B, \omega > 0$, it is easy to see

$$\left|\int_0^t f(t_1)\mathrm{d}t_1\right| = \left|\frac{g\mu_\mathrm{B}B}{2\omega}\sin(\omega t)\right| \le \frac{g\mu_\mathrm{B}B}{2\omega}. \tag{26}$$

According to Eq. (23), the set $\mathcal{S}$ reads

$$\mathcal{S} = \begin{cases} \emptyset, & \frac{g\mu_\mathrm{B}B}{2\omega} < \frac{\Theta}{2}, \\ \{\vec{r}\,|\,\alpha \in [\alpha_f, \pi-\alpha_f]\}, & \frac{g\mu_\mathrm{B}B}{2\omega} \in [\frac{\Theta}{2}, \frac{\pi}{2}], \\ \{\vec{r}\,|\,\alpha \in [\frac{\Theta}{2}, \pi-\frac{\Theta}{2}]\}, & \frac{g\mu_\mathrm{B}B}{2\omega} > \frac{\pi}{2}. \end{cases} \tag{27}$$

Here $\eta \in (0,1]$, $\varphi \in [0, 2\pi]$ and

$$\alpha_f = \arcsin\left(\frac{\sin\left(\frac{\Theta}{2}\right)}{\sin\left(\frac{g\mu_\mathrm{B}B}{2\omega}\right)}\right). \tag{28}$$

Utilizing Theorem 1, Eq. (24) can be written as

$$\int_0^\tau |\cos(\omega t)|\mathrm{d}t = \frac{\Theta}{g\mu_\mathrm{B}B}. \tag{29}$$

In the case that $\frac{g\mu_\mathrm{B}B}{2\omega} < \frac{\Theta}{2}$, $\tau = \infty$ as no states can reach the target. Hence we only consider the non-trivial case that $\frac{g\mu_\mathrm{B}B}{2\omega} \ge \frac{\Theta}{2}$, which means $\frac{\Theta}{g\mu_\mathrm{B}B} \le \frac{1}{\omega}$, and therefore $\int_0^\tau |\cos(\omega t)|\mathrm{d}t \le 1/\omega$, namely, $\int_0^\tau |\cos(\omega t)|\mathrm{d}(\omega t) \le 1$. The integration of $|\cos(\omega t)|$ is only less or equal to 1 when $\omega t \le \pi/2$, in which regime $\cos(\omega t)$ is always non-negative, hence, the integration is equivalent to be performed on $\cos(\omega t)$. Finally, the equation above can be rewritten into

$$\int_0^\tau \cos(\omega t)\mathrm{d}t = \frac{\Theta}{g\mu_\mathrm{B}B}, \tag{30}$$

which immediately gives the analytical expression of τ as below

$$\tau = \frac{1}{\omega}\arcsin\left(\frac{\omega\Theta}{g\mu_\mathrm{B}B}\right). \tag{31}$$

An interesting fact in this case is that the first degenerate point shows at $t = \pi/(2\omega)$, and the OQSL is always less or equal to this time, indicating that the target Θ, regardless of its value, can always be reached before this first degeneracy point.

Next we consider a controlled case that

$$f(t) = -\frac{g\mu_\mathrm{B}}{2}B\cos(\omega t) + u(t), \tag{32}$$

where $|u(t)| \le u_b$ is a bounded control. Since

$$\begin{aligned} &\left|\int_0^t -\frac{g\mu_\mathrm{B}}{2}B\cos(\omega t_1) + u(t_1)\mathrm{d}t_1\right| \\ =&\left|\frac{g\mu_\mathrm{B}B}{2\omega}\sin(\omega t) - \int_0^t u(t_1)\mathrm{d}t_1\right| \\ \le&\frac{g\mu_\mathrm{B}B}{2\omega} + \left|\int_0^t u(t_1)\mathrm{d}t_1\right| \\ \le&\frac{g\mu_\mathrm{B}B}{2\omega} + u_b t, \end{aligned} \tag{33}$$

which can be larger than $\pi/2$ for a long enough time, in this case

$$\mathcal{S} = \left\{\vec{r}\;\middle|\;\alpha \in [\frac{\Theta}{2}, \pi - \frac{\Theta}{2}]\right\}. \tag{34}$$

The OQSL here satisfies

$$\int_0^\tau \left|\frac{g\mu_\mathrm{B}B}{2}\cos(\omega t) - u(t)\right|\mathrm{d}t = \frac{\Theta}{2}. \tag{35}$$

Then the minimum value of τ (denoted by τ_min) can be solved via the problem

$$\tau_\mathrm{min} = \min_{u(t)} \tau, \quad \text{subject to } \begin{cases} \int_0^\tau |\frac{g\mu_\mathrm{B}B}{2}\cos(\omega t) - u(t)|\mathrm{d}t = \frac{\Theta}{2}, \\ |u(t)| \le u_b. \end{cases}$$

This problem can be solved by maximizing the function $|\frac{1}{2}g\mu_\mathrm{B}B\cos(\omega t) - u(t)|$ under the constraint that its integration is fixed. Since $\cos(\omega t)$ is a monotonic function within the regime $[0, \pi/(2\omega)]$, one could have

$$\begin{aligned} &\int_0^{\frac{\pi}{2\omega}} \left|\frac{g\mu_\mathrm{B}B}{2}\cos(\omega t) - u(t)\right|\mathrm{d}t \\ \le&\int_0^{\frac{\pi}{2\omega}} \left[\frac{g\mu_\mathrm{B}B}{2}\cos(\omega t) + u_b\right]\mathrm{d}t \\ =&\frac{g\mu_\mathrm{B}B}{2\omega} + \frac{\pi}{2\omega}u_b. \end{aligned} \tag{36}$$

Notice the condition to make sure $\mathcal{S} \neq \emptyset$ is $\frac{g\mu_\mathrm{B}B}{2\omega} \ge \frac{\Theta}{2}$. In this case, the upper bound of $\int_0^{\frac{\pi}{2\omega}} |\frac{g\mu_\mathrm{B}B}{2}\cos(\omega t) - u(t)|\mathrm{d}t$ is larger than $\Theta/2$, indicating that the integration will reach $\Theta/2$ before the time $\pi/(2\omega)$ with proper controls. Hence, τ_min must be less than $\pi/(2\omega)$. Under this condition, the maximum value of $|\frac{1}{2}g\mu_\mathrm{B}B\cos(\omega t) - u(t)|$ is attained when $u(t) \equiv -u_b$ due to the fact that $\cos(\omega t)$ is

a monotonic function here. Therefore, $\tau_{\min}$ satisfies the equation

$$\frac{g\mu_{\mathrm{B}}B}{2\omega}\sin(\omega\tau_{\min})+u_b\tau_{\min}=\frac{\Theta}{2}. \tag{37}$$

If ω is small, $\tau_{\min}$ approximates to

$$\tau_{\min}\approx\frac{\Theta}{g\mu_{\mathrm{B}}B+2u_b}. \tag{38}$$

C. Example: one-dimensional Ising model with a longitudinal field

1. *Periodic boundary condition*

In the following we consider the one-dimensional Ising model with a longitudinal field. The Hamiltonian of this system reads

$$H/J=-\sum_{j=1}^{n}\sigma_j^z\sigma_{j+1}^z-\sum_{j=1}^{n}g(t)\sigma_j^z, \tag{39}$$

where $J>0$ is the interaction strength of the nearest-neighbor coupling, and $g(t)$ is a global time-dependent longitudinal field. σ_j^z is the Pauli Z matrix for jth spin. The Hamiltonian satisfies the periodic boundary condition $\sigma_{n+1}^z=\sigma_1^z$. Here we only consider the case that $n\geq 3$.

Now we calculate the maximum and minimum eigenvalues of H/J. Since the Hamiltonian only contains the Pauli Z matrix, it is naturally a diagonal matrix in the space consisting of the eigenspaces of σ_j^z for all j. Denote $|\uparrow_j\rangle$ and $|\downarrow_j\rangle$ as the eigenstates of σ_j^z with respect to the eigenvalues 1 and -1, then the eigenvalues of $-\sigma_j^z\sigma_{j+1}^z-g(t)\sigma_j^z$ are $1+g(t)$, $1-g(t)$, $-1-g(t)$, and $-1+g(t)$, and the corresponding eigenstates are $|\downarrow_j\uparrow_{j+1}\rangle$, $|\uparrow_j\downarrow_{j+1}\rangle$, $|\uparrow_j\uparrow_{j+1}\rangle$, and $|\downarrow_j\downarrow_{j+1}\rangle$. The eigenvalues of H/J can be obtained by the summation of a certain number of these four terms. For instance, the eigenvalue with respect to the eigenstate $|\uparrow\rangle^{\otimes n}$ is $\sum_{j=1}^{n}[-1-g(t)]=n[-1-g(t)]$.

Regarding the minimum eigenvalue of H/J, it is easy to see that the minimum eigenvalue of $-\sigma_j^z\sigma_{j+1}^z-g(t)\sigma_j^z$ is $-1-g(t)$ when $g(t)\geq 0$ and $-1+g(t)$ when $g(t)\leq 0$, namely, $-1-|g(t)|$. Therefore, the minimum eigenvalue of H/J is

$$E_{\min,\mathrm{p}}=-n\left[1+|g(t)|\right], \tag{40}$$

which can be attained by the eigenstate $|\uparrow\rangle^{\otimes n}$ when $g(t)\geq 0$ and $|\downarrow\rangle^{\otimes n}$ when $g(t)\leq 0$.

Next, we calculate the maximum eigenvalue. For an eigenstate $\otimes_{j=1}^{n}|a_j\rangle$ $(a_j=\uparrow,\downarrow)$, denote the number of $|\uparrow_j\uparrow_{j+1}\rangle$, $|\downarrow_j\downarrow_{j+1}\rangle$, $|\downarrow_j\uparrow_{j+1}\rangle$, and $|\uparrow_j\downarrow_{j+1}\rangle$ $(j\in[1,N])$ are x_1, x_2, x_3, and x_4, respectively. For example, for the state $|\uparrow\downarrow\uparrow\rangle$, $x_1=1$, $x_2=0$, and $x_3=x_4=1$. Notice

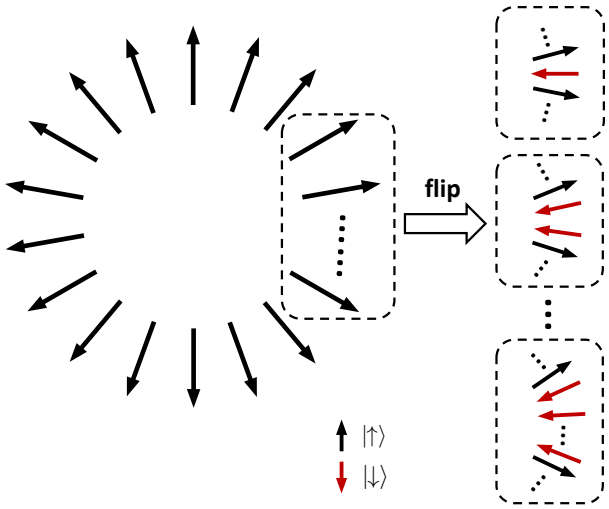

Figure 1. Schematic of obtaining any eigenstate of H/J by flipping any number of $|\uparrow\rangle$ (black up arrow) into $|\downarrow\rangle$ (red down arrow) in the state $|\uparrow\rangle^{\otimes n}$.

that any eigenstate of H/J can be obtained by flipping any number of $|\uparrow\rangle$ in the state $|\uparrow\rangle^{\otimes n}$ into $|\downarrow\rangle$. As long as the number of flipped spins is less than n, no matter how many spins are flipped, there always exists a pair of $|\uparrow\downarrow\rangle$ and $|\downarrow\uparrow\rangle$ at the boundary of the flipped spins, as shown in Fig. 1. For example, assume a flip occurs at the jth spin and k spins are flipped. Then the state of the $(j-1)$th and jth spins must be $|\uparrow_{j-1}\downarrow_j\rangle$, and that of the $(j+k-1)$th and $(j+k)$th spins must be $|\downarrow_{j+k-1}\uparrow_{j+k}\rangle$. If all the spins are flipped, no $|\uparrow\downarrow\rangle$ and $|\downarrow\uparrow\rangle$ exist in the state. The simultaneous existence of $|\uparrow\downarrow\rangle$ and $|\downarrow\uparrow\rangle$ in the flip indicates that x_3 always equals to x_4. Utilizing x_1, x_2, x_3, and the condition $x_1+x_2+2x_3=n$, the eigenvalue of H/J can be expressed by $-[2+g(t)]x_1+[-2+g(t)]x_2+n$. Hence, the calculation of the maximum eigenvalue is equivalent to a linear optimization problem: the maximization of $-[2+g(t)]x_1+[-2+g(t)]x_2+n$ under some constraints on x_1, x_2, and x_3. It is easy to see that the natural constraints on x_1, x_2, and x_3 are $0\leq x_1,x_2\leq n$ and $0\leq x_3\leq\lfloor n/2\rfloor$. Here $\lfloor\cdot\rfloor$ is the floor function. Combing the equation $x_1+x_2+2x_3=n$, the condition $0\leq x_3\leq\lfloor n/2\rfloor$ is equivalent to $0\leq x_1+x_2\leq n$ when n is even and $1\leq x_1+x_2\leq n$ when n is odd, which can be unified as $\frac{1}{2}[1+(-1)^{n+1}]\leq x_1+x_2\leq n$. This condition is fully contained by the constraint $0\leq x_1,x_2\leq n$. Hence, the full linear optimization problem can be expressed by

$$\begin{aligned}&\max_{x_1,x_2}\ -[2+g(t)]\,x_1+[-2+g(t)]\,x_2+n,\\ &\text{subject to }\begin{cases}\eta\leq x_1+x_2\leq n,\\ x_1,x_2\in\mathbb{N}.\end{cases}\end{aligned} \tag{41}$$

Here $\eta:=\frac{1}{2}[1+(-1)^{n+1}]$ and $\mathbb{N}$ is the set of natural numbers.

To solve this problem, four cases have to be discussed:

(1) $g(t) \leq -2$, (2) $-2 < g(t) \leq 0$, (3) $0 < g(t) < 2$, and (4) $g(t) \geq 2$. In the case that $g(t) \leq -2$, the coefficients $-[2+g(t)] \geq 0$ and $-2+g(t) \leq 0$, indicating that the maximum eigenvalue is obtained when x_1 is largest and x_2 vanishes, i.e., $x_1 = n$, $x_2 = 0$. The corresponding maximum eigenvalue is $n[-g(t)-1]$. In the case that $g(t) \in (-2, 0]$, both coefficients $-[2+g(t)]$ and $-2+g(t)$ are negative, and the maximum eigenvalue is attained by the lower bounds of x_1 and x_2. If n is even, the minimum value of x_1 and x_2 are both zero, which leads to the maximum value n. If n is odd, the maximum value is attained by $x_1 = 1$, $x_2 = 0$ due to the fact that $-[2+g(t)]$ is larger than $-2+g(t)$. The corresponding maximum value is $n-2-g(t)$. In the case that $g(t) \in (0, 2)$, the situation is similar to the second one. The maximum value is n and attained by $x_1 = x_2 = 0$ when n is even. For an odd n, the maximum value is $n-2+g(t)$, which can be attained by $x_1 = 0$, $x_2 = 1$. In the last case that $g(t) \geq 2$, $-[2+g(t)] \leq 0$ and $-2+g(t) \geq 0$. The maximum value is $n[g(t)-1]$, which is attained by $x_1 = 0$, $x_2 = n$. In summary, the maximum eigenvalue of H/J is of the form

$$E_{\max,\mathrm{p}} = \begin{cases} n - \eta\left[2 - |g(t)|\right], & |g(t)| < 2, \\ n\left[|g(t)| - 1\right], & |g(t)| \geq 2. \end{cases} \tag{42}$$

Now we consider a specific case that $g(t) = B\cos(\omega t)$, where B is a positive amplitude and ω is the frequency. The OQSL τ is solved via the equation

$$\int_0^\tau E_{\max,\mathrm{p}}(t) - E_{\min,\mathrm{p}}(t)\mathrm{d}t = \Theta. \tag{43}$$

When $B < 2$, $|g(t)|$ is always less than 2, which means $E_{\max,\mathrm{p}}$ always takes the form $n - \eta\left[2 - |g(t)|\right]$, and Eq. (43) reduces to

$$2\left(n-\eta\right)\tau + \left(n+\eta\right)\int_0^\tau |g(t)|\mathrm{d}t = \Theta. \tag{44}$$

For a not very large ω, $\int_0^\tau |g(t)|\mathrm{d}t = \frac{B}{\omega}\sin(\omega\tau) \approx B\tau$. Hence,

$$\tau \approx \frac{\Theta}{2(n-\eta) + B(n+\eta)} =: \tau_1. \tag{45}$$

When $B > 2$, the relation between $|g(t)|$ and 2 is not fixed at different time. However, for a not very large ω, τ is still very small in this case, which means $E_{\max,\mathrm{p}}$ takes the form $n[g(t)-1]$ before the time τ, and $\int_0^\tau |g(t)|\mathrm{d}t$ still approximates to $B\tau$. Therefore, according to Eq. (43), τ approximates to

$$\tau \approx \frac{\Theta}{2Bn} =: \tau_2. \tag{46}$$

The validity of approximation is numerically tested with the changes of amplitude B and frequency ω for different spin number n. As shown in Fig. 2(a), the performance of approximation is very well for different values of B when ω is not extremely large [$\omega/J = 1$ in the plot]. As to the frequency ω, the approximation is valid when ω is no larger than around 10 for both $B = 1.0$ [upper panel in Fig. 2(b)] and $B = 3.0$ (lower panel). As a matter of fact, τ_1 and τ_2 are nothing but the OQSLs for the constant external field $g(t) = B$. Hence, the validity of approximation for a large regime of ω indicates that the OQSL is way more sensitive to the amplitude than the frequency as long as the frequency is not extremely large.

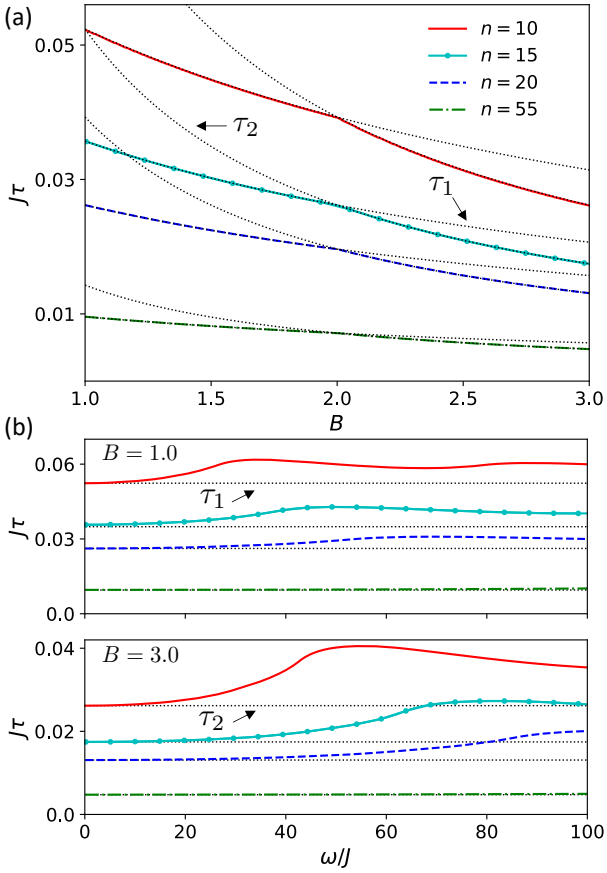

Figure 2. Validity of the approximation with the changes of (a) the amplitude B and (b) the frequency ω for $n = 10$ (solid red lines), $n = 15$ (solid circle cyan lines), $n = 20$ (dashed blue lines), and $n = 55$ (dash-dotted green lines). $\omega/J = 1$ in (a), and in (b) $B = 1.0$ and $B = 3.0$ for the upper and lower panels, respectively.

2. *Open boundary condition*

Next we consider the case of the open boundary condition. The corresponding Hamiltonian reads

$$H/J = -\sum_{j=1}^{n-1}\sigma_j^z\sigma_{j+1}^z - \sum_{j=1}^{n} g(t)\sigma_j^z. \tag{47}$$

In this case, the minimum eigenvalue of $-\sigma_j^z\sigma_{j+1}^z - g(t)\sigma_j^z$ is $-1-g(t)$ $[-1+g(t)]$ for $g(t)\geq 0$ $[g(t)\leq 0]$, which leads to the minimum eigenvalue of H/J

$$E_{\mathrm{min,o}} = -n\left[1+|g(t)|\right]+1. \tag{48}$$

The minimum eigenvalue can be attained by the eigenstate $|\uparrow\rangle^{\otimes n}$ $[|\downarrow\rangle^{\otimes n}]$ for $g(t)\geq 0$ $[g(t)<0]$.

To calculate the maximum eigenvalue, we rewrite the Hamiltonian into the form

$$H/J = H_{\mathrm{p}} + \sigma_n^z\sigma_1^z, \tag{49}$$

where H_{p} is the Hamiltonian under the periodic boundary condition. Now let us denote $E_{\mathrm{max,p}}$ and $|E_{\mathrm{max,p}}\rangle$ as the maximum eigenvalue and corresponding eigenstate of H_{p}, which is actually already obtained in the previous discussion. Notice that the eigenstates of H_{p} are also eigenstates of $\sigma_n^z\sigma_1^z$, and the corresponding eigenvalues can only be 1 and -1. Hence, if $|E_{\mathrm{max,p}}\rangle$ also corresponds to the eigenvalue 1, i.e., $\sigma_n^z\sigma_1^z|E_{\mathrm{max,p}}\rangle = |E_{\mathrm{max,p}}\rangle$, then the maximum energy for the entire Hamiltonian is just $E_{\mathrm{max,p}}+1$. As a matter of fact, this is just the case for any n in the regime $|g(t)|\geq 2$, and for odd n in the regime $|g(t)|<2$. Hence, the maximum eigenvalue E_{max} for these cases reads

$$E_{\mathrm{max,o}} = \begin{cases} n\left[|g(t)|-1\right]+1, & |g(t)|\geq 2, \\ n+|g(t)|-1, & |g(t)|<2 \text{ and } n \text{ is odd}. \end{cases}$$

For an even n in the regime $|g(t)|<2$, $E_{\mathrm{max,p}}-1 = n-1$ may not be the maximum eigenvalue anymore. Another possible candidate must be among the eigenvalues of which the corresponding eigenstate $|E_{\mathrm{c}}\rangle$ satisfies $\sigma_n^z\sigma_1^z|E_{\mathrm{c}}\rangle = |E_{\mathrm{c}}\rangle$. It is obvious that we only need to find the maximum eigenvalues in this case and compare it with $E_{\mathrm{max,p}}-1$. This maximization problem can still be formulated as a linear optimization problem as follows

$$\begin{aligned} &\max_{x_1,x_2} \; -\left[2+g(t)\right]x_1 + \left[-2+g(t)\right]x_2 + n + 1, \\ &\text{subject to } \begin{cases} 2\leq x_1+x_2\leq n, \\ x_1, x_2 \in \mathbb{N}, \\ |g(t)|\leq 2. \end{cases} \end{aligned} \tag{50}$$

The constraint $x_1+x_2\geq 2$ comes from the fact that $\sigma_n^z\sigma_1^z|E_{\mathrm{c}}\rangle = |E_{\mathrm{c}}\rangle$ is equivalent to require $x_1\geq 1$ or $x_2\geq 1$, and $x_1+x_2+2x_3 = n$ requires x_1+x_2 has to be an even number when n is even. Hence, x_1+x_2 has to be no smaller than 2. Since both the coefficients $-[2+g(t)]$ and $-2+g(t)$ are nonpositive in this case, the maximum value must be attained by $x_1=2, x_2=0$ or $x_1=0, x_2=2$. Therefore, in this case the maximum eigenvalue is $n+2|g(t)|-3$. Next we need to compare the value between $n-1$ and $n+2|g(t)|-3$. As a matter of fact, it is easy to see when $n-1$ is larger when $|g(t)|<1$ and $n+2|g(t)|-3$ is larger when $|g(t)|>1$. In summary, the maximum eigenvalue $E_{\mathrm{max,o}}$ under the open boundary condition reads

$$\begin{cases} n-1, & |g(t)|\leq 1 \text{ and } n \text{ is even}, \\ n+2|g(t)|-3, & 1<|g(t)|<2 \text{ and } n \text{ is even}, \\ n+|g(t)|-1, & |g(t)|<2 \text{ and } n \text{ is odd}, \\ n\left[|g(t)|-1\right]+1, & |g(t)|\geq 2. \end{cases} \tag{51}$$

Utilizing the symbol $\eta = [1+(-1)^{n+1}]/2$, the equation above can be rewritten into

$$E_{\mathrm{max,o}} = \begin{cases} n+\eta|g(t)|-1, & |g(t)|\leq 1, \\ n-(2-\eta)[2-|g(t)|]+1, & 1<|g(t)|<2, \\ n\left[|g(t)|-1\right]+1, & |g(t)|\geq 2. \end{cases} \tag{52}$$

Next we calculate the OQSL. In the case that $|g(t)|\leq 1$, τ satisfies the equation

$$(n+\eta)\int_0^\tau |g(t)|\mathrm{d}t + (2n-2)\tau = \Theta. \tag{53}$$

It is easy to see that here $\int_0^\tau |g(t)|\mathrm{d}t$ is less than τ, indicating that

$$\tau \geq \frac{\Theta}{3n-2+\eta}. \tag{54}$$

When $1<|g(t)|<2$, τ satisfies

$$(n+2-\eta)\int_0^\tau |g(t)|\mathrm{d}t + (2n-4+2\eta)\tau = \Theta, \tag{55}$$

which gives

$$\frac{\Theta}{4n} < \tau < \frac{\Theta}{3n-2+\eta} \tag{56}$$

due to the fact that $\tau < \int_0^\tau |g(t)|\mathrm{d}t < 2\tau$. When $|g(t)|\geq 2$, the OQSL satisfies

$$2n\int_0^\tau |g(t)|\mathrm{d}t = \Theta, \tag{57}$$

which means $\tau\leq \Theta/(4n)$.

Let us still consider a specific form of $g(t)$ that $g(t) = B\cos(\omega t)$. Similar to the case with the periodic boundary condition, the approximated expressions of OQSL can also be analytically obtained utilizing the approximation $\int_0^\tau |g(t)|\mathrm{d}t \approx B\tau$ for a not very large ω. In the regime $B\geq 2$, the OQSL is the same with τ_2 [Eq. (46)]. A more interesting phenomenon occurs in the regime $B<2$, where the OQSL is different from τ_1 [Eq. (45)] for an even n. Specifically, the OQSL is

$$\tau \approx \frac{\Theta}{nB+2n-2} =: \tau_3 \tag{58}$$

when $B\leq 1$, and it is

$$\tau \approx \frac{\Theta}{nB+2n+2B-4} \tag{59}$$

when $1 < B < 2$. The maximum gap between the OQSLs for periodic and open boundary conditions happens at the point $B = 0$, i.e., when no external field exists. In this case, the OQSL can be rigorously solved and the difference is

$$\tau_3 - \tau_1 = \frac{\Theta}{2n(n-1)} =: \Delta\tau. \tag{60}$$

The optimal states to realize τ_1 and τ_3 are in the form of Eq. (13). One thing that should be noticed is that the dimension of ξ in the case of periodic boundary condition could be different from that in the case of the open boundary condition due to the different degeneracy of minimum and maximum energies in these two cases.

3. Robustness analysis

The dependence on the boundary condition indicates that the OQSL may be used to detect whether an even-numbered spin ring is ruptured. To do that, one needs to prepare the optimal states in Eq. (12) and then measure $\mathrm{Tr}(\rho_0\rho_t)$ and $\mathrm{Tr}(\rho_t^2)$ at time τ_3 and τ_1, which can be realized via techniques like randomized measurements [2, 3]. Here ρ_0 and ρ_t are the initial state and evolved state at time t. After the measurement, the Bloch angle can be calculated via the equation

$$\cos(\theta(t)) = \frac{\mathrm{Tr}(\rho_0\rho_t) - 2^{-n}}{\sqrt{\left[\mathrm{Tr}(\rho_0^2) - 2^{-n}\right]\left[\mathrm{Tr}(\rho_t^2) - 2^{-n}\right]}}. \tag{61}$$

If the target is fulfilled at time τ_3, then the ring is ruptured, and it is complete if the target is fulfilled at the time τ_1.

A more interesting fact is that the evolution time for the states in Eq. (12) is robust to the global and local dephasing. The global dephasing is described by the master equation

$$\partial_t\rho_t = -i[H, \rho_t] + \gamma_g\left(J_z\rho_t J_z - \frac{1}{2}\left\{\rho_t, J_z^2\right\}\right) \tag{62}$$

with γ_g the decay rate and $J_z = \frac{1}{2}\sum_{j=1}^{n}\sigma_j^z$, and the local dephasing is described by

$$\partial_t\rho_t = -i[H, \rho_t] + \sum_{j=1}^{n}\gamma_{l,j}\left(\sigma_j^z\rho_t\sigma_j^z - \rho_t\right), \tag{63}$$

where $\gamma_{l,j}$ is the decay rate for jth spin.

Now we analytically discuss this robustness under global and local dephasing. We need to emphasize that the optimal states [Eq. (12)] in the noiseless case may not keep optimal when global and local dephasing are involved, and the corresponding evolution time to reach the target may also not be the OQSL anymore. The analysis of OQSL under the noise requires the CRC methodology. Here we only discuss the robustness of the evolution time for the states in Eq. (12).

Recall that the states in Eq. (12) can be written into Eq. (13) in the basis $\{|E_0\rangle, |E_1\rangle, \cdots, |E_{2^n-1}\rangle\}$. Without the external field, the degeneracy of ground states and the highest energy levels are both two. In the meantime, due to the fact that σ_j^z (for any j) and J_z are both diagonal in this basis, we are allowed to denote $J_z = \mathrm{diag}(A, \ldots, G)$ with A and G 2-dimensional diagonal matrices, and $\sigma_j^z = \mathrm{diag}(C_j, \ldots, D_j)$ with C_j and D_j 2-dimensional diagonal matrices. Utilizing these notations, the master equation for global dephasing [Eq. (62)] reduces to the evolution of the block ξ as follows

$$\partial_t\xi_t = i(E_{\max} - E_{\min})\xi_t + \gamma_g A\xi_t G - \frac{\gamma_g}{2}\left(\xi_t G^2 + A^2\xi_t\right), \tag{64}$$

where ξ_t is the evolved block at time t, and the one for local dephasing [Eq. (63)] reduces to

$$\partial_t\xi_t = i(E_{\max} - E_{\min})\xi_t + \sum_j \gamma_{l,j}\left(C_j\xi_t D_j - \xi_t\right). \tag{65}$$

As long as the specific forms of A, G, C_j, and D_j are known, the dynamics can be easily solved. Next, we show the calculations of these blocks.

It is not difficult to see that σ_j^z is easy to be expressed in the basis $\{|\uparrow\rangle, |\downarrow\rangle\}^{\otimes n}$, and the specific forms of σ_j^z (diagonal values) for different values of j are shown in Fig. 3(a), where $\vec{1}_k$ ($-\vec{1}_k$) represents a k-dimensional vector with all entries 1 (-1). To find the expressions of C_j and D_j, we need to know the entry positions of minimum and maximum energies for the Hamiltonian $-\sum_j \sigma_j^z\sigma_{j+1}^z$ and extract the values of σ_j^z in the same positions to reconstruct C_j and D_j. The expression of $-\sigma_j^z\sigma_{j+1}^z$ in the basis $\{|\uparrow\rangle, |\downarrow\rangle\}^{\otimes n}$ for different values of j are given in Fig. 3(b). In this diagram, searching the entry positions of the minimum and maximum energies is equivalent to searching a column with the most number of -1 and 1. It can be seen that the entries of $-\sigma_j^z\sigma_{j+1}^z$ for all values of j are symmetric, indicating that the entire diagram can be divided into four blocks, where the first and fourth (second and third) blocks are mirror symmetric. The positions with respect to the minimum energy are easy to locate since only the first and last entries of $-\sigma_j^z\sigma_{j+1}^z$ are always -1 for all values of j. Hence, their summation (summation of the column in dashed-red boxes) would also be the minimum. In the meantime, the first and last entries of σ_j^z are always 1 and -1 for all values of j, indicating that $C_j = \sigma_z$. Moreover, due to the fact that J_z is half of the summation of all σ_j^z, the entry positions in J_z that correspond to the minimum energy are also the first and last entries, which means $A = \mathrm{diag}(n/2, -n/2) = n\sigma_z/2$.

For the sake of finding the entry positions of the maximum energy, we need to locate the position where the entry is always 1 for any value of j, namely, a column in the diagram where all entries are 1. It is obvious that

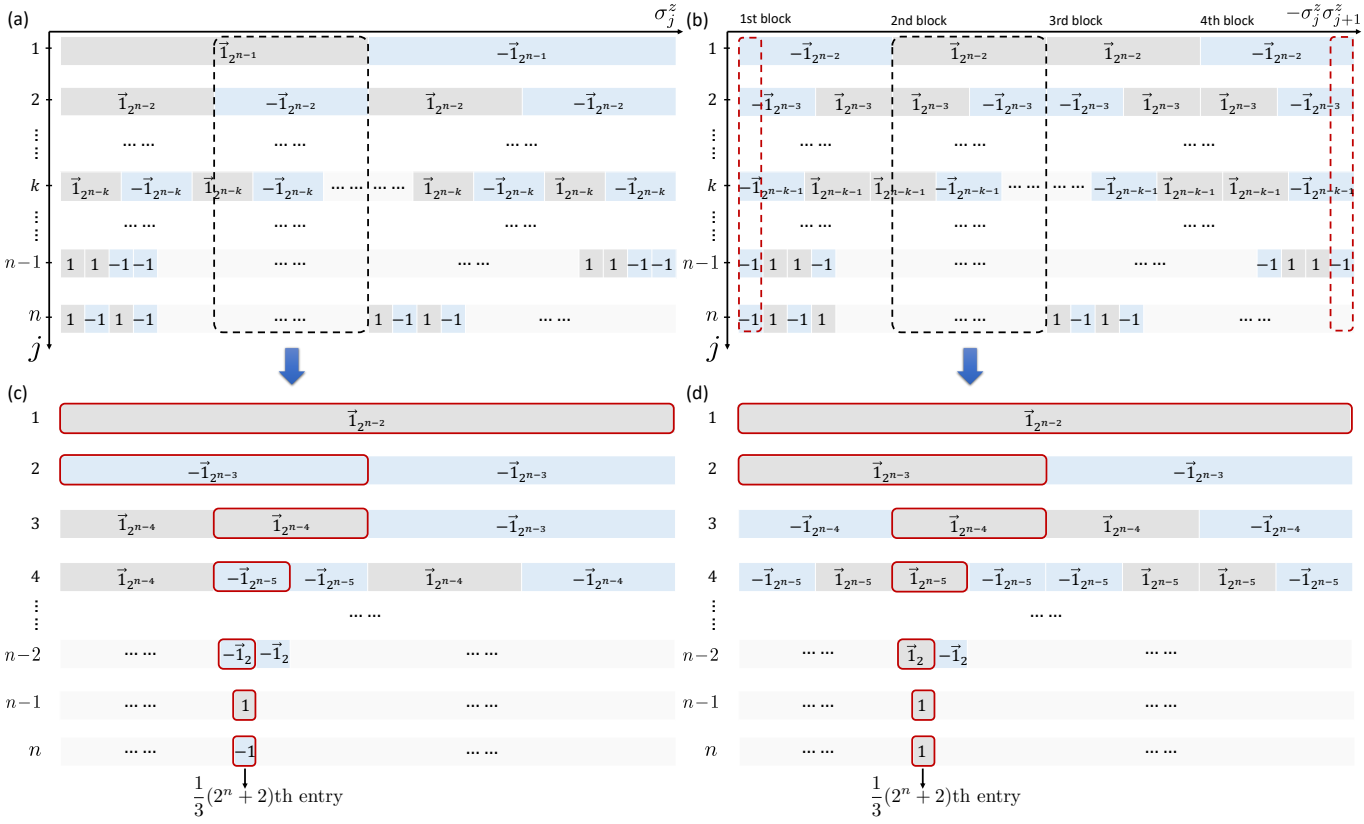

Figure 3. Schematic for the search of entry positions of the minimum and maximum energies. (a) The diagonal entry distribution for σ_j^z; (b) The diagonal entry distribution for $-\sigma_j^z\sigma_{j+1}^z$. [(c),(d)] The second blocks for σ_j^z and $-\sigma_j^z\sigma_{j+1}^z$ for the search of the maximum energy.

it can only exist in the second and third blocks. Due to the symmetry, we only need to consider the second block. As shown in Fig. 3(d), a significant feature in this block is that the overlap between the positions of $\vec{1}$ in the jth and $(j+1)$th lines halves. More specifically to say, compared to the position of $\vec{1}$ in the jth line, only the left (right) half in the same position keeps being 1 in the $(j+1)$th line if j is odd (even). For example, in the first line ($j=1$) all entries are 1, and hence the length of $\vec{1}$ is 2^{n-2}. In the second line ($j=2$), only the left half keeps being one, and the length of $\vec{1}$ becomes 2^{n-3}. Similarly, in the third line ($j=3$) only the right half keeps being 1 compared to the position of $\vec{1}$ in the second line. Utilizing this feature, one can find that when n is even, the $\frac{1}{3}(2^n-1)$th and $\frac{1}{3}(2^n+2)$th entries keep being 1 in the $(n-2)$th line. Notice that the entry number here starts from the beginning of all diagonal entries of $-\sigma_j^z\sigma_{j+1}^z$, not the beginning of the second block. And in the $(n-1)$th line, the $\frac{1}{3}(2^n+2)$th entry is 1. In the case of open boundary condition, this is the last line and the position is located. In the case of the periodic boundary condition, one more line of $-\sigma_n^z\sigma_1^z$ needs to be considered. Luckily, this position of $-\sigma_n^z\sigma_1^z$ is also 1 when n is even. Therefore, the maximum energy is at the $\frac{1}{3}(2^n+2)$th entry under both boundary conditions. Due to the symmetry, the $\frac{1}{3}(2^{n+1}+1)$th entry, which is in the third block, is also maximum.

Now we locate the values of $\frac{1}{3}(2^n+2)$th and $\frac{1}{3}(2^{n+1}+1)$th entries in σ_j^z, which is irrelevant to the boundary condition. The block of entries in σ_j^z with respect to the second block in Fig. 3(b) is given in Fig. 3(c). As shown in this diagram, the $\frac{1}{3}(2^n+2)$th entry is 1 for an odd j and -1 for an even j, namely, it is $(-1)^{j+1}$. Similarly, one can find that the $\frac{1}{3}(2^{n+1}+1)$th entry is $(-1)^j$. Hence, $D_j=(-1)^{j+1}\sigma_z$. In the meantime, both $\frac{1}{3}(2^n+2)$th and $\frac{1}{3}(2^{n+1}+1)$th entries are zero in J_z when n is even, which means $G=0$.

In summary, we have found that $A=n\sigma_z/2$, $G=0$, $C_j=\sigma_z$, and $D_j=(-1)^{j+1}\sigma_z$. Utilizing these expressions, Eqs. (64) and (65) can be further written into

$$\partial_t\xi_t=\left[i(E_{\max}-E_{\min})-\frac{n^2\gamma_g}{8}\right]\xi_t, \tag{66}$$

and

$$\partial_t\xi_t=i(E_{\max}-E_{\min})\xi_t+\sum_j\gamma_{l,j}\left[(-1)^{j+1}\sigma_z\xi_t\sigma_z-\xi_t\right]. \tag{67}$$

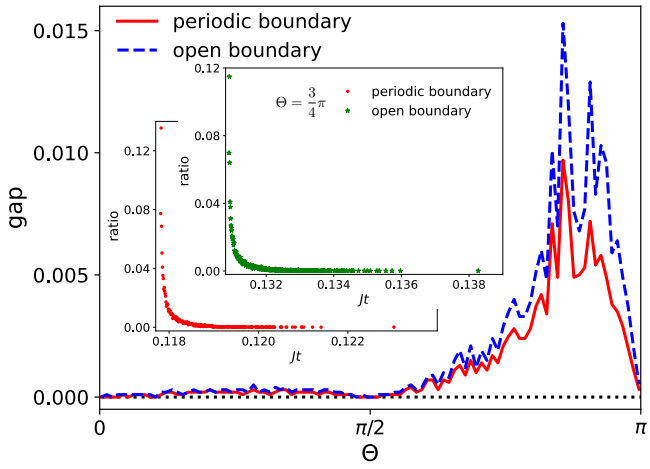

Figure 4. The variety of the gap between the maximum and minimum values of the evolution time to reach the target Θ among 100 random states with random values of $\{\gamma_{l,j}\} \in (0,1)$. The insets present the ratios of 10000 states at different evolution time to reach the target $\Theta = 3\pi/4$ for periodic (red dots) and open (green pentagrams) boundary conditions. $n = 10$ in all plots.

Equation (66) can be easily solved as

$$\xi_t = e^{\left[i(E_{\max}-E_{\min})-\frac{n^2\gamma_g}{8}\right]}\xi, \tag{68}$$

and Eq. (67) can be solved as

$$\begin{aligned}[\xi_t]_{00(11)} =& e^{i(E_{\max}-E_{\min})-\sum_{j=1}^{n}\gamma_{l,j}\left[1+(-1)^j\right]}[\xi]_{00(11)},\\ [\xi_t]_{01(10)} =& e^{i(E_{\max}-E_{\min})-\sum_{j=1}^{n}\gamma_{l,j}\left[1-(-1)^j\right]}[\xi]_{01(10)}.\end{aligned}$$

Here $[\cdot]_{ab}$ represents the abth entry $(a,b=0,1)$.

Next we calculate $\cos(\theta(t))$. Notice that Eq. (61) can be expressed by

$$\cos(\theta(t)) = \frac{\mathrm{Re}\left(\mathrm{Tr}(\xi\xi_t^\dagger)\right)}{\sqrt{\mathrm{Re}\left(\mathrm{Tr}(\xi\xi^\dagger)\right)\mathrm{Re}\left(\mathrm{Tr}(\xi_t\xi_t^\dagger)\right)}}, \tag{69}$$

where $\mathrm{Re}(\cdot)$ represents the real part. In the case of global dephasing [Eq. (66)], the expression above reduces to

$$\cos(\theta(t)) = \cos\left((E_{\max}-E_{\min})t\right), \tag{70}$$

which is irrelevant to the decay rate γ. Hence, the evolution time to reach the target for the optimal states in Eq. (13) is indeed robust to the global dephasing in both periodic and open boundary conditions, indicating that their difference is also robust.

In the case of local dephasing, Eq. (69) can be expressed by

$$\begin{aligned}&\cos(\theta(t))\\ &= \cos\left((E_{\max}-E_{\min})t\right)\frac{\varsigma_1+\varsigma_2 e^{-2t\gamma_{\mathrm{all}}}}{\sqrt{\varsigma_1+\varsigma_2}\sqrt{\varsigma_1+\varsigma_2 e^{-4t\gamma_{\mathrm{all}}}}},\end{aligned}$$

where $\varsigma_1 = |[\xi_t]_{00}|^2 + |[\xi_t]_{11}|^2$, $\varsigma_2 = |[\xi_t]_{01}|^2 + |[\xi_t]_{10}|^2$, and $\gamma_{\mathrm{all}} = \sum_{j=1}^{n}\gamma_{l,j}(-1)^j$. If the values of all decay rates $\{\gamma_{l,j}\}$ are very close, for example $\gamma_{l,j} \approx \gamma$ for any j, then $\gamma_{\mathrm{all}} \approx 0$ and $\cos(\theta(t))$ still approximates to $\cos\left((E_{\max}-E_{\min})t\right)$, which is also irrelevant to the decay rates, and thus in this case the evolution time, as well as the time difference, are also robust to the local dephasing. In the case that the values of $\{\gamma_{l,j}\}$ are not close, Eq. (69) is indeed dependent on the decay rates. However, since $\varsigma_1 + \varsigma_2 e^{-2t\gamma_{\mathrm{all}}}$ is always positive at finite time, the evolution time is still irrelevant to γ_{all} for the target $\Theta = \pi/2$ and hence robust to the local dephasing. For a general target, we have tested 100 random states in Eq. (13) with random values of $\{\gamma_{l,j}\} \in (0,1)$ for each target in the case of $n = 10$, and the gap between the maximum and minimum values of the evolution time for these 100 states are given in Fig. 4. It can be seen that the robustness is quite good when the target is no larger than $\pi/2$, and it is indeed compromised when Θ is larger than $\pi/2$. Even for those targets with large gaps, the evolution time for different states could concentrate on some specific values, namely, the distribution of states in the gap has a sharp peak. For example, the insets of Fig. 4 show the distributions of 10000 states for periodic (red dots) and open (green pentagrams) boundary conditions in the case of $\Theta = 3\pi/4$. It can be seen that the distributions for both periodic and open boundary conditions have a sharp peak at the minimum values, indicating that the evolution time is still relatively robust for most states.

II. LEARNING THE OQSL IN LANDAU-ZENER MODEL

A. Verification of the validity of CRC methodology

Here we present the process of learning the OQSL in the Landau-Zener model and show the validity of the CRC methodology. The Hamiltonian of this model is

$$H = \Delta\sigma_x + vt\sigma_z, \tag{71}$$

where Δ and v are two time-independent parameters. σ_x and σ_z are the Pauli matrices. The OQSL in this model has been thoroughly discussed in Ref. [1], in which the set $\mathcal{S}$ is obtained via the brute-force search among around one million pure states. The reason why only pure states are considered here is due to the fact that unitary evolution does not affect the purity and in the Bloch representation all states in the same direction can/cannot reach the target simultaneously. The dynamics is solved via QuTiP [4, 5]. The full evolution is truncated at $vt = 10$, namely, the state is treated to not be in $\mathcal{S}$ if it cannot reach the target within the truncated time. The Bloch vector of the initial state is parameterized by

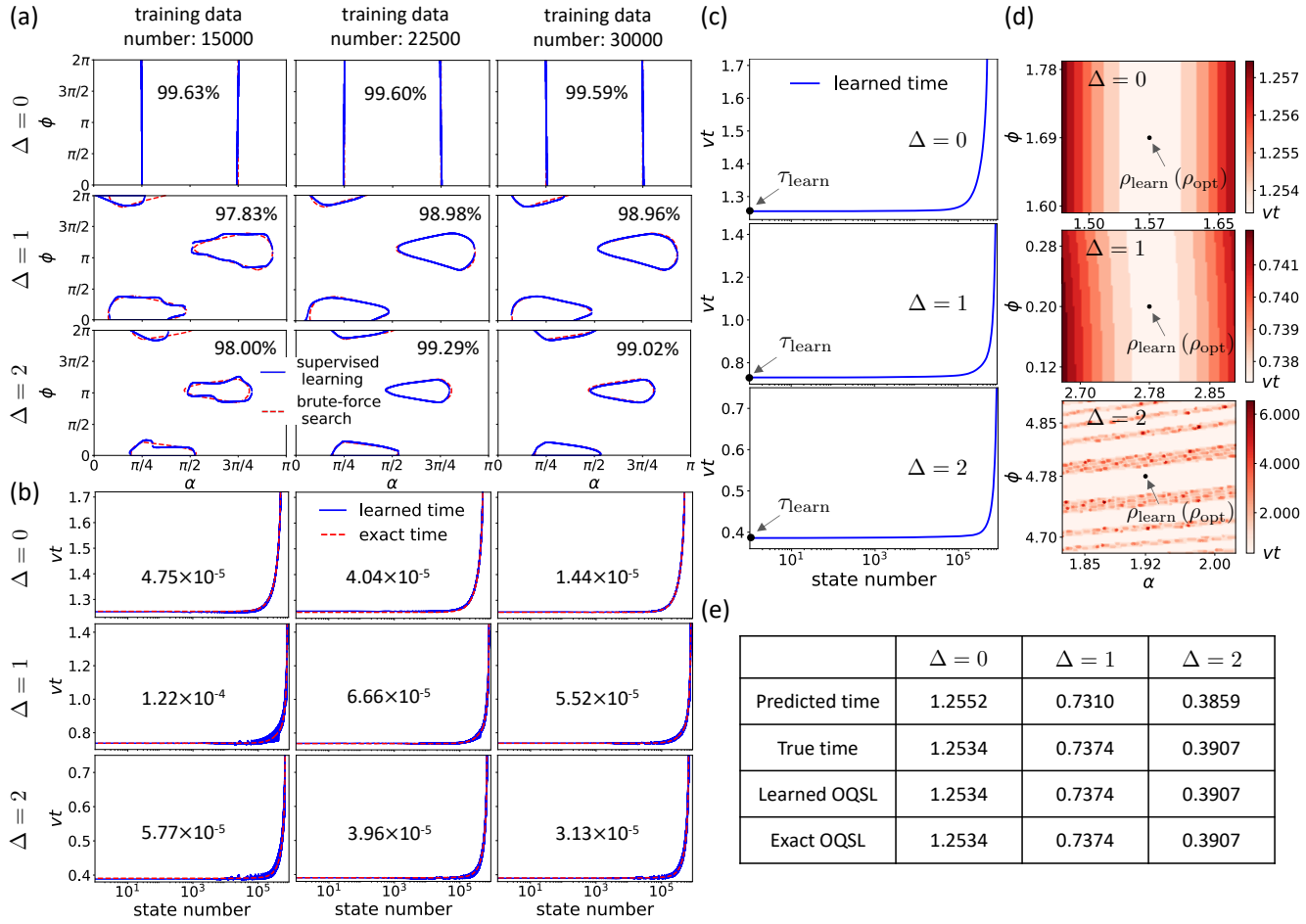

	$\Delta = 0$	$\Delta = 1$	$\Delta = 2$
Predicted time	1.2552	0.7310	0.3859
True time	1.2534	0.7374	0.3907
Learned OQSL	1.2534	0.7374	0.3907
Exact OQSL	1.2534	0.7374	0.3907

Figure 5. (a) Comparison between the set $\mathcal{S}$ (brute-force search) and $\mathcal{S}_{\text{learn}}$ (learning) with different values of Δ and different training data number. The first, second, and third rows represent the results for $\Delta = 0$, $\Delta = 1$, and $\Delta = 2$, respectively. The first, second, and third columns represent the results for 15000, 22500, and 30000 training data, respectively. The solid blue (dashed red) lines represent the boundaries between $\mathcal{S}$ ($\mathcal{S}_{\text{learn}}$) and its complementary set. The percentage numbers in the plots are the scores of the learning. (b) Comparison of the evolution time to reach the target obtained from the regression process (solid blue lines) and the exact time obtained from the brute-force search (dashed red lines). Here the input states in the regression are the ones in $\mathcal{S}$. The numbers in the plots are the mean square errors of learning. (c) The practical performance of the regression process where the input states are those in $\mathcal{S}_{\text{learn}}$. (d) Results of the calibration process. The region for calibration is taken as $[\alpha_{\text{learn}} - 0.1, \alpha_{\text{learn}} + 0.1]$ and $[\phi_{\text{learn}} - 0.1, \phi_{\text{learn}} + 0.1]$. The black dots represent $(\alpha_{\text{learn}}, \phi_{\text{learn}})$, the "optimal" points obtained in the regression. (e) Table of the predicted time (τ_{learn}) obtained in the practical regression process, the corresponding true time, and finally learned OQSL after the calibration process for different values of Δ. The exact OQSL is obtained via brute-force search. In all plots v is set to be 1 and the target angle $\Theta = \pi/2$.

$\vec{r} = (\sin\alpha\cos\phi, \sin\alpha\sin\phi, \cos\alpha)^{\mathrm{T}}$ with $\alpha \in [0, \pi]$ and $\phi \in [0, 2\pi)$.

In the step of classification, a multilayer neural network with two inputs (α and ϕ) and one output (1 or 0) is created with a hyperbolic tangent function as the activation function. The output result 1/0 represents that the input initial state can/cannot realize the given target, respectively. Supervised learning is performed via scikit-learn [6]. The network contains five to six hidden layers each with about 200 to 250 neurons. The Cross-Entropy loss function [7] is used as the loss function, and Adam [8] is applied in the updates of the network. The test set contains all the initial states (around one million states) used in the brute-force search. The performance of training for different values of Δ are given in Fig. 5(a). The first, second, and third rows represent the learned $\mathcal{S}$ for $\Delta = 0$, $\Delta = 1$, and $\Delta = 2$ (in the units of $\sqrt{v}$). The solid blue and dashed red lines represent the boundaries between $\mathcal{S}$ and its complementary set obtained via supervised learning and brute-force search. Different numbers of the training set, including 15000, 22500, and 30000, have also been tested and compared, as shown in the first (15000), second (22500), and third (30000) columns in Fig. 5(a). The percentage numbers in the plots are the scores of learning, i.e., the correctness of the network's output. It can be seen that the performance of

15000 training data is better than the others in the case of $\Delta = 0$, and 22500 training data present the best performance in the cases of $\Delta = 1$ and $\Delta = 2$. One should notice that all the parameters of the network are manually tuned case by case, and the slight difference in the performance may not be fully due to the difference in the training data number. In the case of 22500 training data, the correctness is around 99%, indicating that about 0.99 million states are correctly classified into $\mathcal{S}$ and its complementary set. Therefore, the neural network indeed works for the classification in this example.

The second step is the regression process, in which basically the same neural network is created but with rectified linear unit function as the activation function. The loss function is taken as the square error loss function [9]. The training data are sorted by the evolution time to reach the target from smallest to largest. Similar to the classification process, all the states in $\mathcal{S}$ are used to test the performance of the network. Notice that $\mathcal{S}$ here is the exact reachable state set obtained via the brute-force search since we need to check the validity of the network. The performance of regression is presented for different values of Δ and training data number in Fig. 5(b). All the plots in this figure are semi-logarithmic (x axis). The first, second, and third rows represent the results for $\Delta = 0$, $\Delta = 1$, and $\Delta = 2$. The first, second, and third columns represent the results for 15000, 22500, and 30000 training data. The number in the plots are the mean square errors of learning, i.e., $\frac{1}{m}\sum_{i=1}^{m}\left[t_{\text{pre}}^{(i)} - t_{\text{ext}}^{(i)}\right]^2$. Here $t_{\text{pre}}^{(i)}$ and $t_{\text{ext}}^{(i)}$ are the predicted time obtained via learning and exact time obtained via brute-force search for the ith state. The order of states in the figure is sorted by the evolution time obtained in the brute-force search from smallest to largest, and the learned time is plotted using the same order of states. Notice that these states are not exactly the same for different values of Δ due to the dependence of $\mathcal{S}$ on Δ. It can be seen that the performance of learning (solid blue lines) is good for all values of Δ, especially when the training data number is 22500 and 30000. Basically the mean square errors of learning in these two cases for all values of Δ are in the scale of 10^{-5}. Hence, the network also works for the regression in this example.

As a matter of fact, in practice the reachable state set used in the regression process is the one obtained in the classification process (denoted by $\mathcal{S}_{\text{learn}}$). Hence, although it is reasonable to use the true $\mathcal{S}$ to check the validity of the regression, $\mathcal{S}_{\text{learn}}$ has to be applied to test if the OQSL obtained from CRC methodology is reasonable. The performance of regression with respect to $\mathcal{S}_{\text{learn}}$ for 22500 training data is given in Fig. 5(c) for different values of Δ. The results for the other two training data numbers are not shown here due to their similarity. Since the training set chosen in Fig. 5(b) is also a subset of $\mathcal{S}_{\text{learn}}$, we can directly use it as the training set in this case and the trained network is then the same. The states in the plots are sorted by the evolution time to reach the target from smallest to largest. As shown in this figure, the trend of learned time basically coincides with the exact time in Fig. 5(b). One should notice that in fact these two lines cannot be compared directly as the states are not exactly the same. Utilizing the result of the regression, the "optimal" state ρ_{learn} and corresponding predicted time τ_{learn} can be located. The rigorous evolution time of ρ_{learn} to reach the target (true time) is given in the table in Fig. 5(e). It can be seen that the predicted time τ_{learn} is very close to the true time for all values of Δ. The errors in all cases are on the scale of 10^{-3}, indicating that the regression process works well in this example. Furthermore, the true time of ρ_{learn} coincides with the exact OQSL obtained via brute-force search, which means ρ_{learn} is indeed an optimal state in this case.

The last process is calibration. The core of this process is to calculate the rigorous dynamics of the states around ρ_{learn} and find the exact minimum time in this region. This process guarantees the finally obtained time is the rigorous minimum time in this region. In this example, the values of (α, ϕ) for the "optimal" states [denoted by $(\alpha_{\text{learn}}, \phi_{\text{learn}})$] in the cases of $\Delta = 0$, $\Delta = 1$, and $\Delta = 2$ are $(1.57, 1.69)$, $(2, 78, 0.20)$, and $(1.92, 4.78)$, respectively [black dots in Fig. 5(d)]. The region to perform the calibration is $[\alpha_{\text{learn}} - 0.1, \alpha_{\text{learn}} + 0.1]$ and $[\phi_{\text{learn}} - 0.1, \phi_{\text{learn}} + 0.1]$. The rigorous dynamics of about 10000 states in this region are calculated. The results are given in Fig. 5(d) and the corresponding minimum time (learned OQSL) is given in the table in Fig. 5(e). The consistency between the learned OQSL and the exact OQSL proves that the final result is indeed the exact OQSL in this example. The validity of the CRC methodology is then confirmed.

B. Learning the OQSL in the controlled system

Next, we apply the CRC methodology to search the OQSL in the controlled Landau-Zener model. The full Hamiltonian of this model reads

$$H = \Delta\sigma_x + vt\sigma_z + \vec{u}\cdot\vec{\sigma}, \tag{72}$$

where $\vec{\sigma} = (\sigma_x, \sigma_y, \sigma_z)$ is the vector of Pauli matrices, and $\vec{u} = (u_x, u_y, u_z)$ is the vector of control amplitudes.

We first discuss the generation of controls for a specific initial state to reach the target at the minimum time. The controls are generated via the auto-GRAPE [10] with the objective function

$$f = \int_0^T \cos\left(\theta(t)\right) \mathrm{d}t, \tag{73}$$

where T is a reasonably long time (truncated time in our calculation), and $\theta(t)$ is the angle between the Bloch vec-

Algorithm 1: auto-GRAPE

Initialize the control amplitude $u_k(t)$ for all t and k;
for episode=1, M **do**
  Receive initial state ρ_0;
  for $t = 1, T$ **do**
    Evolve with the control $\rho_t = e^{\Delta t \mathcal{L}_t}\rho_{t-1}$;
    Calculate $f_t = \frac{N\mathrm{Tr}(\rho_0\rho_t)-1}{\sqrt{[N\mathrm{Tr}(\rho_0^2)-1][N\mathrm{Tr}(\rho_t^2)-1]}}$ and save it;
  end for
  Calculate the objective function $f = \sum_t f_t$.
  Calculate the gradient $\frac{\delta f}{\delta u_k(t)}$ with the automatic differentiation method for all t and k.
  for $t = 1, T$ **do**
    for $k = 1, K$ **do**
      Update control $u_k(t) \leftarrow u_k(t) + \epsilon \frac{\delta f}{\delta u_k(t)}$.
    end for
  end for
end for
Save the controls $\{u_k\}$.

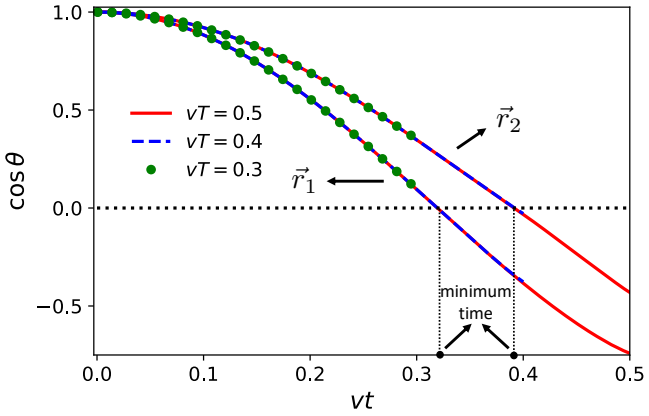

Figure 6. Performance of controls for two randomly generated initial states $\vec{r}_1$ and $\vec{r}_2$ with different values of T (in the unit of v), including $T = 0.3$ (green dots), $T = 0.4$ (dashed blue lines), and $T = 0.5$ (solid red lines).

tors of initial state ρ_0 and its evolved state ρ_t, which satisfies the equation $\partial_t\rho_t = \mathcal{L}_t\rho_t$ with $\mathcal{L}_t$ a time-dependent superoperator. Notice that in the Bloch representation the density matrix can be expressed by Eq. (3). Then $\cos(\theta(t))$ can be calculated by

$$\cos(\theta(t)) = \frac{N\mathrm{Tr}(\rho_0\rho_t) - 1}{\sqrt{[N\mathrm{Tr}(\rho_0^2) - 1]\,[N\mathrm{Tr}(\rho_t^2) - 1]}}. \tag{74}$$

In this case, the dynamics is unitary and only pure states need to be calculated, then $\cos(\theta(t))$ reduces to $2\mathrm{Tr}(\rho_0\rho_t) - 1$. In the numerical calculation, the evolution time is usually discretized into many equally spaced time points ($\{t_i\}$), and thus we can use the discrete form

$$f = \sum_i \cos(\theta(t_i)) \tag{75}$$

as the objective function instead. The time interval here is neglected since it does not affect the final performance.

Auto-GRAPE is a gradient-based algorithm where the gradient is evaluated via automatic differentiation [10]. In Ref. [10] the quantum metrological quantities like quantum Fisher information are taken as the objective function, here in this paper we take Eq. (75) as the objective function. The corresponding pseudocode is given in Algorithm 1. In one episode, the initial state is evolved to time T and the objective function is calculated. Then the gradients $\delta f/\delta u_k(t)$ for all t and k are evaluated via automatic differentiation, which is realized with the Julia package Zygote [11]. At last, all the control amplitudes are updated simultaneously according to the evaluation of gradients. In practice, Adam [8] could be applied to further improve efficiency.

To test the validity of the objective function [Eq. (75)], the performance of corresponding controls are demonstrated in Fig. 6 for two randomly generated initial states, of which the Bloch vectors are $(0.22, 0.20, -0.96)^{\mathrm{T}} := \vec{r}_1$ and $(0.95, -0.15, -0.29)^{\mathrm{T}} := \vec{r}_2$. Three different values of T (in the unit of v), including $T = 0.3$ (green dots), $T = 0.4$ (dashed blue lines), and $T = 0.5$ (solid red lines) are tested. As shown in the figure, the optimal controls for $T = 0.4$ and 0.5 can let the states reach the target angle (dotted black line) at the same time, confirming that this found time (black dots) is indeed minimum. In the meantime, if T is smaller than the minimum time, for example $T = 0.3$, the states cannot reach the target angle during the entire evolution, which also corroborates that the found time is minimum as the states cannot reach the target before this time. Hence, the validity of the objective function and corresponding controls are confirmed. Moreover, the consistency of performance for $T = 0.4$ and $T = 0.5$ shows that the choice of T does not affect the result of minimum time as long as it is larger than the minimum time.

Next, we perform the CRC methodology for $\Delta = 0, 1, 2, 3, 4, 5, 6$ (in the units of $\sqrt{v}$) in both noiseless and noisy cases. In the noiseless case, the result of classification shows that all states in the state space can fulfill the target. This phenomenon is reasonable in physics due to the full controllability of $\vec{u}\cdot\vec{\sigma}$, which means the controls can realize the rotation of a state from any angle. Thus, any state can fulfill the target in finite time under this control Hamiltonian even without the free Hamiltonian $\Delta\sigma_x + vt\sigma_z$.

In the step of regression, the data number of training and test sets are 22500 and 7500. Similar to the noncontrolled case, the mean square errors between the learned time (solid blue lines) and exact time (dashed red lines) in the test set are still on the scales of 10^{-5} and 10^{-6} for all values of Δ, as shown in the left column in Fig. 7(a). Utilizing this learned regression network, about one million states are input and corresponding learned time (solid

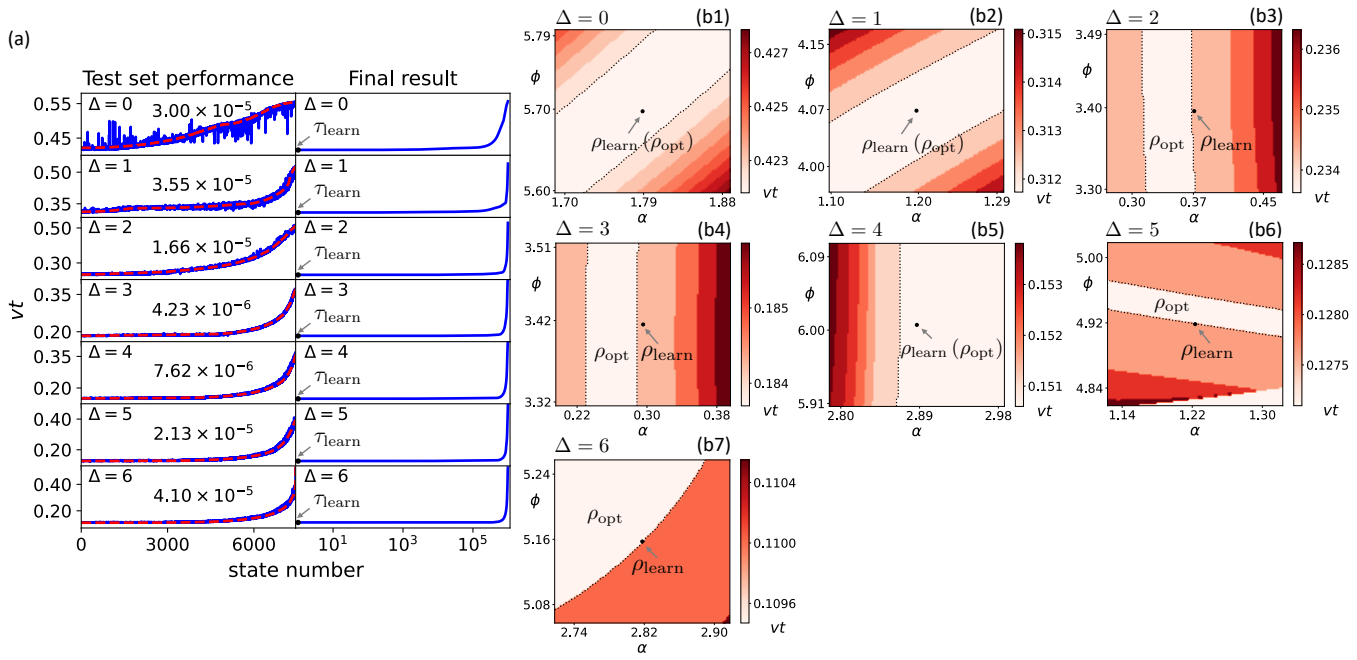

Figure 7. CRC methodology for controlled noiseless dynamics. (a) The left column: The test set performance of the regression process for $\Delta = 0, 1, 2, 3, 4, 5, 6$ (top to bottom). The right column: The result of regression for $\Delta = 0, 1, 2, 3, 4, 5, 6$ (top to bottom). The solid blue and dashed red lines represent the learned time and exact time obtained from regression and rigorous dynamics, respectively. The numbers in the left column are the mean square errors of learning. The x axes in both columns are in the logarithmic scales. [(b1)-(b7)] Results of calibration for $\Delta = 0, 1, 2, 3, 4, 5, 6$. The regime for calibration is $[\alpha_{\rm learn} - 0.1, \alpha_{\rm learn} + 0.1]$ and $[\phi_{\rm learn} - 0.1, \phi_{\rm learn} + 0.1]$. The target Θ is taken as $\pi/2$ in all plots.

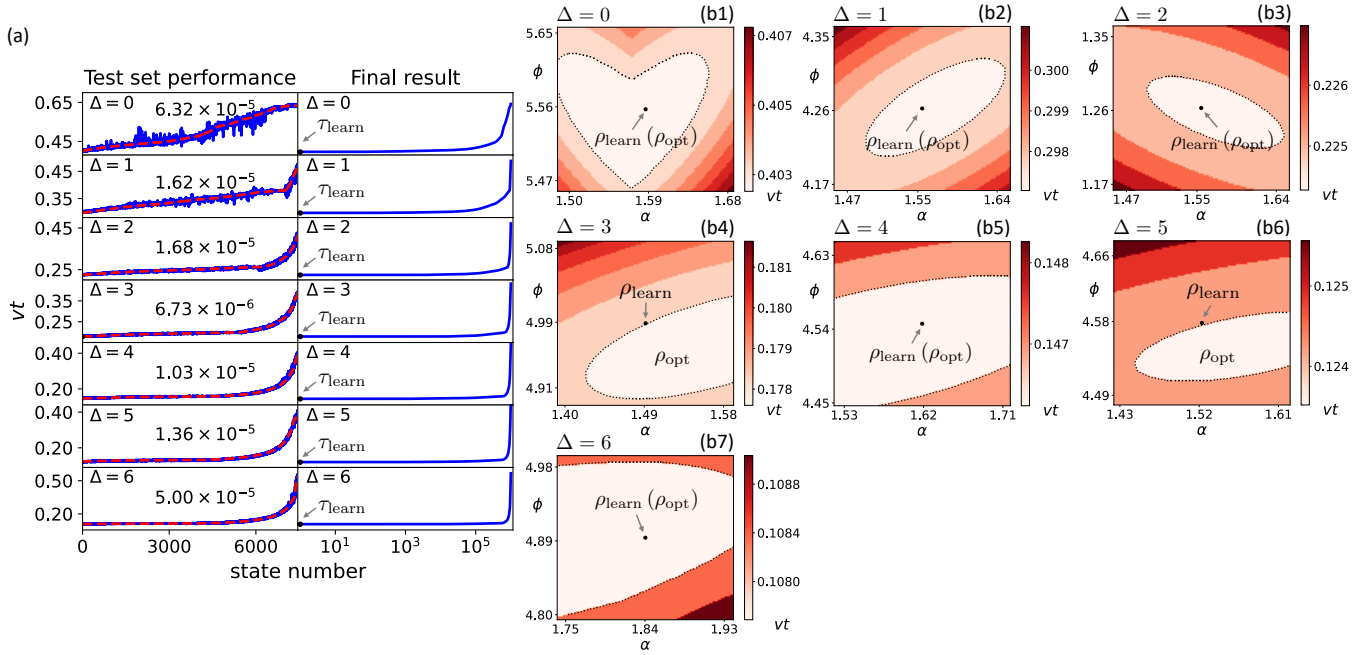

Figure 8. CRC methodology for controlled noisy dynamics. (a) The left column: The test set performance of the regression process for $\Delta = 0, 1, 2, 3, 4, 5, 6$ (top to bottom). The right column: The result of regression for $\Delta = 0, 1, 2, 3, 4, 5, 6$ (top to bottom). The solid blue and dashed red lines represent the learned time and exact time obtained from regression and rigorous dynamics, respectively. The numbers in the left column are the mean square errors of learning. The x axes in both columns are in the logarithmic scales. [(b1)-(b7)] Results of calibration for $\Delta = 0, 1, 2, 3, 4, 5, 6$. The regime for calibration is $[\alpha_{\rm learn} - 0.1, \alpha_{\rm learn} + 0.1]$ and $[\phi_{\rm learn} - 0.1, \phi_{\rm learn} + 0.1]$. The target Θ is taken as $\pi/2$ in all plots.

blue lines) is given in the right column in Fig. 7(a). The minimum time $\tau_{\rm learn}$ for $\Delta = 0, 1, 2, 3, 4, 5, 6$ are 0.4154, 0.3080, 0.2315, 0.1830, 0.1486, 0.1261, and 0.1113, respectively.

In the last step, the region for calibration is still taken as $[\alpha_{\rm learn}-0.1, \alpha_{\rm learn}+0.1]$ and $[\phi_{\rm learn}-0.1, \phi_{\rm learn}+0.1]$. The results of calibration are given in Figs. 7(b1)-7(b7). As shown in the plots, the optimal state $\rho_{\rm opt}$ coincides with $\rho_{\rm learn}$ in the cases of $\Delta = 0, 1, 4$. However, the position of $\rho_{\rm opt}$ slightly moves away from $\rho_{\rm learn}$ in other cases, which proves the necessity of the step of calibration.

In the noisy case, the dephasing is invoked and the dynamics of the density matrix is governed by the master equation

$$\partial_t \rho_t = -i[H, \rho_t] + \gamma(\sigma_z \rho_t \sigma_z - \rho_t), \tag{76}$$

where the Hamiltonian is in Eq. (72) and γ is the decay rate, which is taken as $0.5\sqrt{v}$ in the following calculation. The CRC methodology has been applied in this case for $\Delta = 0, 1, 2, 3, 4, 5, 6$ (in the units of $\sqrt{v}$). The result of the classification here is the same as that in the noiseless case, i.e., all states can fulfill the target under control. The results of regression and calibration are given in Fig. 8. Similar to the noiseless case, the mean square errors of regression are still on the scales of 10^{-5} and 10^{-6}, as shown in Fig. 8(a). The minimum time $\tau_{\rm learn}$ for $\Delta = 0, 1, 2, 3, 4, 5, 6$ are 0.3961, 0.2968, 0.2242, 0.1783, 0.1440, 0.1196, and 0.1063, respectively. In the calibration, the region for calibration is still taken as $[\alpha_{\rm learn}-0.1, \alpha_{\rm learn}+0.1]$ and $[\phi_{\rm learn}-0.1, \phi_{\rm learn}+0.1]$, as shown in Figs. 8(b1)-8(b7) for different values of Δ. The results show that $\rho_{\rm opt}$ are either the same with $\rho_{\rm learn}$, or very close to it, indicating that both regression and calibration processes are effective in this case.

III. THE OQSL FOR TRANSVERSE ISING MODEL

In this section we show the OQSL in the case of the one-dimensional transverse Ising model, of which the Hamiltonian is

$$H/J = -\sum_{j=1}^{n} \sigma_j^z \sigma_{j+1}^z - g(t) \sum_{j=1}^{n} \sigma_j^x, \tag{77}$$

where J is the interaction strength between the qubits, and $g(t)$ is the time-dependent strength of the external field. Here we consider that $g(t) = B\cos(\omega t)$.

Because of the enormous state space for this Hamiltonian, it is not easy to set up good training sets that are general enough for the CRC methodology. To feasibly apply the CRC methodology, we need to analyze the state structure first and reduce the state space for the study. A simple way to categorize the states is based on the number of nonzero entries in a certain basis. Therefore, we analyze the evolution time to reach the target for the states with different numbers of nonzero entries in the basis $\{|\uparrow\rangle, |\downarrow\rangle\}^{\otimes n}$. Here $|\uparrow\rangle$ ($|\downarrow\rangle$) is the eigenvalue of σ_z with respect to the eigenvalue 1 (-1). The evolution time to reach the target has been calculated for 2000 random states in each category, and the minimum time is given in Fig. 9. It can be seen that the minimum time for the states with 2 (dotted-red-pentagram line) and 3 (dashed-green-cross line) nonzero entries is always lower than that for the states with 10 (solid-blue-triangle line) nonzero entries when n is no larger than 100. This phenomenon indicates that in this example we only need to focus on the states with few nonzero entries for the study of OQSL.

In the meantime, we found an interesting phenomenon.

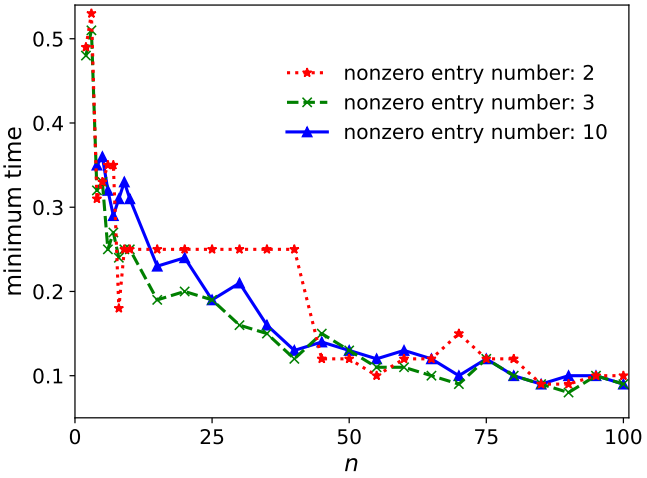

Figure 9. The minimum time to reach the target as a function of spin number n for 2000 random states with 2 nonzero entries (dotted-red-pentagram line), 3 nonzero entries (dashed-green-cross line), and 10 nonzero entries (solid-blue-triangle line). The parameters are set as $\Theta = \pi/2$, $B = 0.5$, and $\omega/J = 1$.

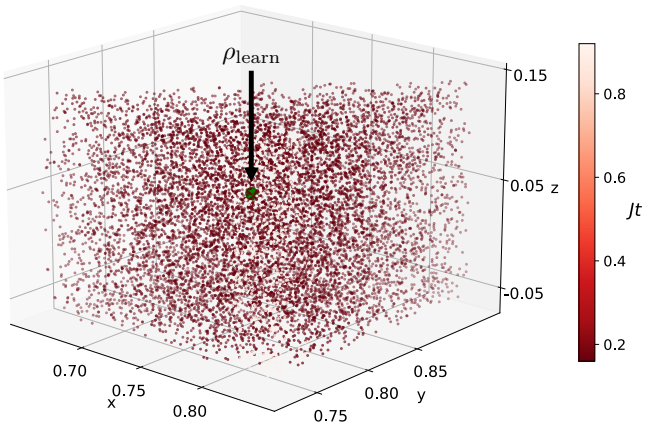

Figure 10. Calibration result in the category of states with 2 nonzero entries. The green dot is the position of $\rho_{\rm learn}$.

nonzero entry number	classification		regression			calibration
	score	ratio	mean square error	τ_{learn}	true value	optimal time
2	94.55%	7.71%	8.95×10^{-4}	0.24	0.19	0.18
3	89.67%	5.85%	2.06×10^{-2}	0.18	0.25	0.24
4	85.44%	6.73%	1.69×10^{-2}	0.52	0.37	0.36
5	81.52%	9.48%	1.54×10^{-2}	0.54	0.24	0.24

Table I. Results of CRC methodology in the categories of 2, 3, 4, and 5 nonzero entries.

The ratio of reachable states in the 2000 random states basically fits the function

$$\frac{1}{1+an^be^{-cn^d}}. \tag{78}$$

The parameters a, b, c, d are 1.132, 1.309, 0.005, 1.826 for the category of 2 nonzero entries, and 0.450, 1.654, 0.034, 1.355 for the category of 3 nonzero entries, and 0.613, 0.842, 0.007, 1.754 for the category of 10 nonzero entries. The true ratio in this case and the physical mechanism behind it are still open questions and need to be further investigated in the future.

Next, we perform the CRC methodology to evaluate the OQSL. Since we only need to focus on the states with few nonzero entries, the CRC methodology is applied in the categories of states with 2, 3, 4, and 5 nonzero entries. The results are given in Table I. In all cases, 22500 and 7500 states and corresponding results (0 or 1) consist of the training and test sets in the classification process. The best score of the trained network we obtain is 94.55%, 89.67%, 85.44%, and 81.52% in the categories of 2, 3, 4, and 5 nonzero entries. The results show that 7.71%, 5.85%, 6.73%, and 9.48% states can fulfill the target in these categories. In the regression process, we also use 22500 and 7500 states and the corresponding evolution time to reach the target as the training and test sets. The best mean square errors of the trained network we obtain are 8.95×10^{-4}, 0.0206, 0.0169, and 0.0154 in the categories of 2, 3, 4, and 5 nonzero entries, and corresponding values of τ_{learn} are 0.24, 0.18, 0.52, and 0.54. The true values of the evolution time of ρ_{learn} are 0.19, 0.25, 0.37, and 0.24. The gap between τ_{learn} and the true values are majorly affected by the mean square errors, and it becomes difficult to obtain a good mean square error with the increase of the nonzero entry number. About 10000 random states in the neighborhood of ρ_{learn} are used in the process of calibration. These states share the same positions of nonzero entries with ρ_{learn} and the differences of the norms and phases between them and ρ_{learn} are less than 0.1. The calibration in the category of 2 nonzero entries is shown in Fig. 10. The x and y axes are the norms of the nonzero entries and the z axis is the phase difference between these two entries. The green dot is the position of ρ_{learn}. The other three categories are not shown since the parameters are larger than 3. After the calibration, the optimal evolution time in these categories is 0.18, 0.24, 0.36, and 0.24. Hence, the final evaluation of OQSL in this example is 0.18, which can be realized by certain states with 2 nonzero entries.

* liujingphys@hust.edu.cn

[1] Y. Shao, B. Liu, M. Zhang, H. Yuan, and J. Liu, Operational definition of a quantum speed limit, Phys. Rev. Research **2**, 023299 (2020).

[2] S. J. van Enk and C. W. J. Beenakker, Measuring Trρ^n on Single Copies of ρ Using Random Measurements, Phys. Rev. Lett. **108**, 110503 (2012).

[3] A. Elben, B. Vermersch, R. van Bijnen, C. Kokail, T. Brydges, C. Maier, M. K. Joshi, R. Blatt, C. F. Roos, and P. Zoller, Cross-Platform Verification of Intermediate Scale Quantum Devices, Phys. Rev. Lett. **124**, 010504 (2020).

[4] J. R. Johansson, P. D. Nation, and F. Nori, QuTiP: An open-source Python framework for the dynamics of open quantum systems, Comp. Phys. Comm. **183**, 1760 (2012).

[5] J. R. Johansson, P. D. Nation, and F. Nori, QuTiP 2: A Python framework for the dynamics of open quantum systems, Comp. Phys. Comm. **184**, 1234 (2013).

[6] F. Pedregosa, G. Varoquaux, A. Gramfort, V. Michel, B. Thirion, O. Grisel, M. Blondel, P. Prettenhofer, R. Weiss, V. Dubourg, J. Vanderplas, A. Passos, D. Cournapeau, M. Brucher, M. Perrot, and É. Duchesnay, Scikit-learn: Machine Learning in Python, J. Mach. Learn. Res. **12**, 2825 (2011).

[7] E. B. Baum and F. Wilczek, *Supervised learning of probability distributions by neural networks* (American Institute of Physics, New York, 1988).

[8] D. P. Kingma and J. Ba, Adam: A Method for Stochastic Optimization, arXiv:1412.6980.

[9] E. L. Lehmann and G. Casella, *Theory of Point Estimation* (Springer, New York, 1998).

[10] M. Zhang, H.-M. Yu, H. Yuan, X. Wang, R. Demkowicz-Dobrzański, and J. Liu, QuanEstimation: An open-source toolkit for quantum parameter estimation, Phys. Rev. Research **4**, 043057 (2022).

[11] M. Innes, Don't Unroll Adjoint: Differentiating SSA-form programs, arXiv:1810.07951.